

Original Article

NANOCARRIER-ENCAPSULATED SGLT-2 INHIBITOR (DAPAGLIFLOZIN) PROTECTS AGAINST DIABETIC CARDIOMYOPATHY BY REDUCING MYOCARDIAL FIBROSIS

C.Y. Li¹, F. Xu², L.R. Zhu², C. Cheng², J.Y. Kuang³ and T. Zhao^{2,*}¹Department of Gynecology, Shandong Provincial Hospital Affiliated to Shandong First Medical University, 250021 Jinan, Shandong, China²Department of Cardiology, The Second Hospital of Shandong University, 250033 Jinan, Shandong, China³Central Research Laboratory, The Second Hospital of Shandong University, 250033 Jinan, Shandong, China

Abstract

Background: Diabetic cardiomyopathy (DCM) is a common complication in diabetic patients and often leads to the onset of heart failure (HF). Nanoparticle (NP) drug delivery systems are a therapeutic approach that have a potential therapeutic value for improving diabetic HF. This study aims to evaluate the therapeutic effects of NP-loaded sodium-glucose cotransporter-2 (SGLT-2) inhibitors, such as dapagliflozin (DAPA), on HF induced by DCM and elucidate the underlying mechanisms of action. **Methods:** DAPA nanoscale formulation was prepared. DCM model mice and AC16 cells were treated with different formulations of DAPA (free DAPA, DAPA@poly(lactic-co-glycolic acid) (PLGA), DAPA@PLGA-thioetheral (TK)-polyethylene glycol (PEG)). The extent of myocardial damage in mice was assessed through staining with hematoxylin-eosin, Masson, and Sirius red. Levels of superoxide dismutase (SOD), catalase (CAT), glutathione (GSH), malondialdehyde (MDA), protein carbonyl (PCO), total iron, and Fe²⁺ were determined through enzyme-linked immunosorbent assay (ELISA) and UV spectrophotometry. Expression levels of transferrin receptor protein 1 (TfR1) and ferroportin (FPN) proteins in the DCM mouse and high-glucose cell models were measured through Western blot. Reactive oxygen species (ROS) levels in AC16 cells were assessed using fluorescent probes. Changes in mitochondrial damage and membrane potential were evaluated by transmission electron microscopy and 5,5',6,6'-tetrachloro-1,1',3,3'-tetraethyl-imidacarbocyanine (JC-1) fluorescent dye. **Results:** DAPA@NPs have an average diameter of 66.1 nm and a zeta potential of 16.5 mV. At 2.5 mg DAPA, the best encapsulation efficiency (86.11 ± 0.49 %) and load capacity (3.82 ± 2.11 %) were obtained. In the DCM model, DAPA@NPs significantly up-regulated the levels of SOD and CAT in oxidative stress indices, and significantly down-regulated the levels of PCO and MDA ($p < 0.001$). In addition, DAPA@NPs significantly up-regulate adenosine triphosphate (ATP) levels ($p < 0.001$) and alleviate mitochondrial damage. Finally, DAPA@NPs inhibit iron death by down-regulating total iron and Fe²⁺ levels, inhibiting TfR1 expression, up-regulating GSH level, and promoting FPN expression ($p < 0.001$). **Conclusions:** DAPA@NPs may treat diabetic HF by inhibiting myocardial fibrosis, reducing oxidative stress, preserving mitochondrial function, and regulating cardiac iron metabolism.

Keywords: Dapagliflozin, nanocarrier, diabetic cardiomyopathy, myocardial fibrosis, oxidative stress.

***Address for correspondence:** T. Zhao, Department of Cardiology, The Second Hospital of Shandong University, 250033 Jinan, Shandong, China. Email: zhaotongzbw@163.com.

Copyright policy: © 2025 The Author(s). Published by Forum Multimedia Publishing, LLC. This article is distributed in accordance with Creative Commons Attribution Licence (<http://creativecommons.org/licenses/by/4.0/>).

Introduction

Diabetic cardiomyopathy (DCM) represents a significant cardiovascular complication in patients with diabetes mellitus and is characterized by structural and functional abnormalities in the myocardium independent of coronary artery disease or hypertension [1,2]. Among various pathophysiological mechanisms implicated in DCM, myocardial fibrosis plays a pivotal role and contributes to myocardial stiffness, diastolic dysfunction, and ultimately heart failure [3,4]. According to Vergès [5], patients with type 1 diabetes (T1D) have a significantly increased cardiovascular

risk. A large observational study conducted in Scotland between 2005 and 2007 in T1D patients aged 20 years or older showed that the age-adjusted incidence ratio for a first cardiovascular disease event was 2.34 for men and 3.02 for women compared with the non-diabetic population. In addition, the degree of cardiac fibrosis assessed by cardiac magnetic resonance imaging (MRI) was associated with increased mortality and heart failure-related hospitalizations in patients with diabetes mellitus type 2 (T2DM) [6]. To date, there is no consensus on the best management strategy to prevent or treat diabetes-related cardiovascular compli-

Table 1. EE % and LC % of DAPA within the NPs.

	Encapsulation efficiency (EE %)	Load capacity (LC %)
DAPA@NP (2.5 mg)	86.11 ± 0.49	3.82 ± 2.11
DAPA@NP (5 mg)	52.18 ± 0.65	3.41 ± 1.82
DAPA@NP (7.5 mg)	49.52 ± 0.56	3.04 ± 1.93
DAPA@NP (10 mg)	19.21 ± 0.39	1.38 ± 0.96

DAPA, dapagliflozin; NP, nanoparticle.

cations. Current treatment options for patients with type 1 diabetes mellitus or type 2 diabetes mellitus aim to treat insulin resistance, reduce inflammation, and reduce oxidative stress [7].

Sodium-glucose cotransporter-2 (SGLT-2) inhibitors have emerged as a promising class of drugs for the management of diabetes primarily by promoting glycosuria and reducing hyperglycemia [8,9]. In addition to their glycemic control effects, SGLT-2 inhibitors have demonstrated pleiotropic cardiovascular benefits, including improvements in myocardial metabolism, oxidative stress, inflammation, and fibrosis [10,11]. However, the direct effects of SGLT-2 inhibitors on myocardial fibrosis in the context of DCM and the underlying mechanisms remain incompletely understood.

In recent years, nanotechnology-based drug delivery systems have garnered increasing attention for their potential to enhance drug efficacy, improve tissue targeting, and minimize adverse effects [12,13]. Encapsulation of pharmacological agents within nanocarriers offers a promising approach to overcome limitations associated with conventional drug delivery methods and enhance therapeutic outcomes [14,15]. Poly(lactic-co-glycolic acid) nanoparticles (PLGA NPs), as a drug delivery vehicle, have many advantages: continuous and controlled delivery of treatment and minimization of concentration fluctuations in the systemic circulation, continuous release of the drug by using low levels of the required drug dose, and reduced frequency of administration and fluctuations in the responses of the immune system to the drug [16].

This study aims to investigate the protective effects of a novel nanocarrier encapsulating SGLT-2 inhibitor dapagliflozin (DAPA) against myocardial fibrosis in DCM. The nanocarrier, designed using state-of-the-art nanotechnology, facilitates the targeted delivery of DAPA to the myocardium, thereby maximizing its therapeutic effects while minimizing systemic side effects. The molecular mechanisms underlying the reduction of myocardial fibrosis by nanoencapsulated DAPA were elucidated. This study aims to provide novel insights into the treatment of DCM and potentially identify new therapeutic targets.

Materials and Methods

Design, Preparation, and Characterization of DAPA@NP

Poly(lactic-co-glycolic acid) (PLGA) or PLGA-thioketal (TK)-polyethylene glycol (PEG) and DAPA were

dissolved in dimethyl sulfoxide (DMSO)/deionized water in a 1:2 ratio [17]. The drug-polymer solution was added to an aqueous phase containing the emulsifier polyvinyl alcohol (PVA), and ultrasonic processing was conducted to form an oil-in-water (O/W) emulsion. The emulsion was stirred under reduced pressure to evaporate the organic solvent and form a nanoparticle (NP) suspension. The nanoparticles were isolated from the suspension through high-speed centrifugation and rinsed with deionized water to eliminate any remaining emulsifier and free drug. The nanoparticles were freeze dried to ensure their stability for extended storage. The size and morphology of the nanoparticles were characterized by transmission electron microscopy (TEM, spectra 300, Thermo Fisher Scientific, Waltham, MA, USA) and dynamic light scattering (DLS, ZS90, Malvern Instrument, Great Malvern, UK) analyses. High performance liquid chromatography-ultraviolet (HPLC-UV) method (detection wavelength 260 nm, mobile phase A: ddH₂O, mobile phase B: acetonitrile 30–70 %) was used to detect the encapsulation efficiency (EE %) and load capacity (LC %).

$EE \% = (\text{Actual amount of encapsulated drug} / \text{Initial amount of drug loaded}) \times 100 \%$.

$LC \% = (\text{Total weight of nanoparticles} / \text{Actual amount of encapsulated drug}) \times 100 \%$.

A laser particle size analyzer (3000+ Ultra, Mastersizer, Malvern Panalytical, Malvern, UK) was employed to determine the particle size, polydispersity index, and zeta potential of DAPA@NPs. The shape and structure of the nanoparticles were examined using a transmission electron microscope (JEM-2100, JEOL, Tokyo, Japan).

DAPA@PLGA and DAPA@PLGA-TK-PEG were placed into membranes with a molecular weight cutoff of 10 kDa and dialyzed in phosphate buffer saline (PBS) solution (pH 6.5 and pH 7.4, which represent the pH of blood and the tumor microenvironment) [18] at 37 °C with agitation. In addition, 100 μM H₂O₂ was administered to simulate the tumor microenvironment [19]. Dialysis was conducted at a certain speed. Nanoparticles in the dialysis bag had a concentration of 1 mg/mL, with a total volume of 5 mL. The surrounding release medium had a volume of 50 mL. At specified intervals, 3 mL of the release medium was sampled, and an equal volume of fresh dialysis buffer was added. The concentration of DAPA in the collected release medium was then analyzed using a UV-2600 UV-visible spectrophotometer (Shimadzu, Kyoto, Japan).

DCM Animal Model

Male C57BL/6J mice (6–8 weeks old, weighing 18–20 g) were obtained from Shanghai MODEL ORGANISMS (Shanghai, China). The mice were kept in a pathogen-free environment with an ambient temperature of 23 ± 2 °C, humidity of 55 ± 5 %, and a 12-hour light/dark cycle. They had free access to food and water. The mice received a single intraperitoneal injection of 1 % streptozotocin (STZ, 150 mg/kg, HY-13753, MedChemExpress, South Brunswick, NJ, USA). Blood samples were taken from the tail veins on days 3, 5, and 7 after injection, and blood glucose levels were measured using a glucometer. Mice with blood glucose levels ≥ 16.7 mmol/L were selected as diabetic models and were maintained for 4 weeks to develop DCM. The mice were then randomly assigned to five groups:

Control group: Healthy mice received oral saline.

Model group: DCM mice were treated with saline for 6 weeks.

Free DAPA group: DCM mice received 20 mg/kg/day of DAPA for 6 weeks.

DAPA@PLGA group: DCM mice received 20 mg/kg/day of DAPA@PLGA for 6 weeks.

DAPA@PLGA-TK-PEG group: DCM mice received 20 mg/kg/day of DAPA@PLGA-TK-PEG for 6 weeks.

At the end of the treatment period, all mice were euthanized with an intraperitoneal injection of pentobarbital sodium (3 mg/mL, 110 mg/kg). Fresh sterile heart tissues were collected for analysis, and blood was drawn through pericardiocentesis. The blood samples were centrifuged at 4500 g (4 °C) for 15 minutes to separate the serum.

Cell Culture

Human cardiomyocytes (AC16 cells) (iCell-h323) were purchased from iCell Inc. (Shanghai, China) and cultured in specialized AC16 cell culture medium (iCell-h323-001b) at 37 °C with 5 % CO₂. In this study, AC16 cells were subjected to a high glucose concentration of 35 mmol/L for 24 hours to establish an *in vitro* model of DCM. The AC16 cells were subjected to short tandem repeat (STR) identification and tested negative for mycoplasma contamination.

Histopathology

Tissue specimens were fixed and dehydrated. For hematoxylin-eosin (HE) staining (G1120, Solarbio, Beijing, China), the specimens were immersed in hematoxylin to stain the nuclei, followed by washing in acidic alcohol to remove excess dye. The specimens were stained with eosin to color the cytoplasm. After dehydration and clearing steps, the specimens were mounted in a transparent medium for microscopic examination. For Masson's trichrome staining (G1340, Solarbio, Beijing, China), the specimens were treated similarly with hematoxylin for nuclear staining, followed by acid alcohol washing. The specimens were stained with acidic fuchsin to color colla-

gen fibers red, followed by aniline blue to stain cytoplasm green. Following washing, dehydration, and clearing, the specimens were mounted for microscopy. For Sirius red staining, the specimens were immersed in Sirius red dye (G1472, Solarbio, Beijing, China) to stain collagen fibers red, followed by washing, dehydration, and clearing. The specimens were then mounted for microscopic observation (BX53, Olympus, Tokyo, Japan). These staining methods are commonly employed in pathology and biological research to assess tissue structure, histology, and fibrosis levels.

Transmission Electron Microscopy

The left ventricular tissue specimens were fixed in 2.5 % glutaraldehyde solution (P1126, Solarbio, Beijing, China). The fixed tissue specimens were embedded in epoxy resin and acrylic resin and then sliced into ultrathin sections (approximately 1 mm) by using an ultramicrotome. The morphology, structure, and distribution of muscle fibers and mitochondria were observed using a transmission electron microscope (JEM-1400, JEOL, Tokyo, Japan).

CCK-8 Assay

AC16 cells were seeded into culture dishes and cultured under conditions of 37 °C and 5 % CO₂ until reaching the logarithmic growth phase. The cells were then exposed to different forms of DAPA for 24 hours (Free DAPA, DAPA@PLGA, DAPA@PLGA-TK-PEG) (10 mM). Subsequently, cell counting kit-8 (CCK-8) solution (CA1210, Solarbio, Beijing, China) was added to each group of cell cultures. The culture dishes were placed in a CO₂ incubator at 37 °C for 2 hours. After the incubation, the absorbance of each group of cell cultures was measured using a microplate reader (EnVision, PerkinElmer, Wellesley, MA, USA) at a wavelength of 450 nm. Cell viability was calculated based on the absorbance values of each group.

Biochemical Analysis

Malondialdehyde (MDA) (S0131S), protein carbonyl (PCO) (VT000038), glutathione (GSH) (S0073), and adenosine triphosphate (ATP, S0026) assay kits were acquired from Beyotime (Shanghai, China). Acquired Fe²⁺ (BC5415) and total iron (BC2865) assay kits were purchased from Solarbio (Beijing, China). All experiments were conducted according to the manufacturer's instructions, and measurements were performed using a UV-visible spectrophotometer (UV-2600, Shimadzu, Kyoto, Japan).

Measurement of Enzyme Activities

The procedures for assessing the activities of layered double hydroxides (LDH) (BC0685), catalase (CAT) (BC0205), superoxide dismutase (SOD) (BC5165), and glutathione peroxidase (GSH-Px) (BC1195) were carried

out using specific assay kits (Solarbio, Beijing, China). Each experiment adhered to the protocols provided by the manufacturer, with measurements obtained using an En-Vision microplate reader (PerkinElmer, Wellesley, MA, USA).

Fluorescent Staining

Cells were stained with 2',7'-dichlorodihydrofluorescein diacetate (DCFH-DA, D6470, Solarbio, Beijing, China), boron-dipyrromethene (BODIPY)TM 581/591 C11 (D3861, Invitrogen, Carlsbad, CA, USA), and 5,5',6,6'-tetrachloro-1,1',3,3'-tetraethylimidacarbocyanine (JC-1, J8030, Invitrogen, Carlsbad, CA, USA) fluorescent dyes. Working solutions of each dye were prepared according to the manufacturer's instructions typically by diluting the stock solution in an appropriate buffer or culture medium. The cells were incubated with the respective dye working solutions for a certain duration at an optimal temperature to allow the uptake of the fluorescent dyes by the cells in a dark environment. After incubation, the cells were washed with buffer or medium to remove any excess dye and impurities. Finally, the stained cells were analyzed using fluorescence microscopy (IX83, Olympus, Tokyo, Japan) to observe the fluorescence signals indicative of cellular characteristics, such as reactive oxygen species (ROS) levels (DCFH-DA staining), lipid peroxidation (BODIPY 581/591 C11 staining), or mitochondrial membrane potential (JC-1 staining). Staining conditions, including dye concentration, incubation time, and temperature, should be optimized for each specific experiment to ensure reliable results.

Western Blot Analysis

A lysis buffer (R0010, Solarbio, Beijing, China) was used to extract proteins from the cell cultures or tissue samples. The concentration of the extracted proteins was determined using bicinchoninic acid assay (BCA) method (PC0020, Solarbio, Beijing, China). The protein samples were loaded into wells of a polyacrylamide gel (SDS-PAGE gel) and subjected to electrophoresis for separation. The separated proteins were transferred from the sodium dodecyl sulfate polyacrylamide gel electrophoresis (SDS-PAGE) gel onto a polyvinylidene fluoride membrane (PVDF) (YA1701, Solarbio, Beijing, China). Bovine serum albumin was added to the proteins on the membrane to prevent nonspecific binding. Primary antibodies transferrin receptor protein 1 (TfR1, 1:1000, ab214039, Abcam, Cambridge, MA, USA), ferroportin (FPN, 1:1000, ab78066, Abcam, Cambridge, MA, USA), and glyceraldehyde-3-phosphate dehydrogenase (GAPDH) (1:1000, ab8245, Abcam, Cambridge, MA, USA) were added to the membrane to bind to the target protein. Secondary antibodies conjugated to a detectable marker were added onto the membrane to bind to the primary antibodies. The membrane was washed to remove unbound secondary antibody (1:1000,

ab6721, Abcam, Cambridge, MA, USA). Target proteins on the membrane were detected using an imaging system (Chemidoc MP Imaging System, Bio-Rad Laboratories, Helsingør, CA, USA). The protein bands were analyzed and quantified using Image J software (version 1.53e, National Institutes of Health, Bethesda, MD, USA).

Statistical Analysis

Data are expressed as mean \pm SD. Differences between two groups were analyzed using *T*-test, while comparisons among multiple groups were made using one-way analysis of variance (ANOVA). Tukey's test was applied for post-hoc analysis. Statistical evaluations were conducted with GraphPad Prism software (version 9.0, GraphPad Software, San Diego, CA, USA). A *p*-value of less than 0.05 was considered statistically significant.

Results

Characterization of DAPA@NPs

The TEM images (Fig. 1A) reveal that DAPA@NPs are regularly spherical with smooth surfaces, indicating successful synthesis. The average diameter of the nanoparticles is 66.1 nm (Fig. 1B). The zeta potential of DAPA@NPs is 16.5 mV (Fig. 1C). Table 1 presents the drug load capacity (LC %) and encapsulation efficiency (EE %) of DAPA within the nanoparticles. Optimal encapsulation efficiency (86.11 \pm 0.49 %) and loading capacity (3.82 \pm 2.11 %) were obtained by adjusting the polymer to DAPA ratio, with 2.5 mg of DAPA. We compared the drug release rates of nanoparticles based on thioketal (TK) (DAPA@PLGA-TK-PEG) and PLGA (DAPA@PLGA) at different pH levels (6.5 and 7.4) in solution (Fig. 1D,E). In pH 6.5 solution, DAPA@PLGA-TK-PEG exhibited a cumulative release of 83.21 % within 48 hours, compared with 73.56 % for DAPA@PLGA. At pH 7.4, the release rates were 85.23 % for DAPA@PLGA-TK-PEG and 59.31 % for DAPA@PLGA. In addition, H₂O₂ was administered to simulate the tumor high-ROS microenvironment (Fig. 1F). The release rates of DAPA@PLGA and DAPA@PLGA-TK-PEG are 66.47 and 83.47, respectively. These results indicate that DAPA@PLGA-TK-PEG has superior drug release capabilities.

DAPA@NP Alleviates Fibrosis and Oxidative Stress in Diabetic Myocardial Tissue

A dilated cardiomyopathy (DCM) mouse model was established to evaluate the therapeutic efficacy of DAPA@NPs in diabetic heart failure. Pathological staining was employed to assess myocardial injury severity. Hematoxylin-eosin (HE) staining (Fig. 2A) revealed that myocardial fibers were intact and organized in the control group. In the model group, myocardial fibers appeared disordered or ruptured, accompanied by increased necrosis and inflammatory cell infiltration, resulting in blurred myocardial patterns. However, treatment with dif-

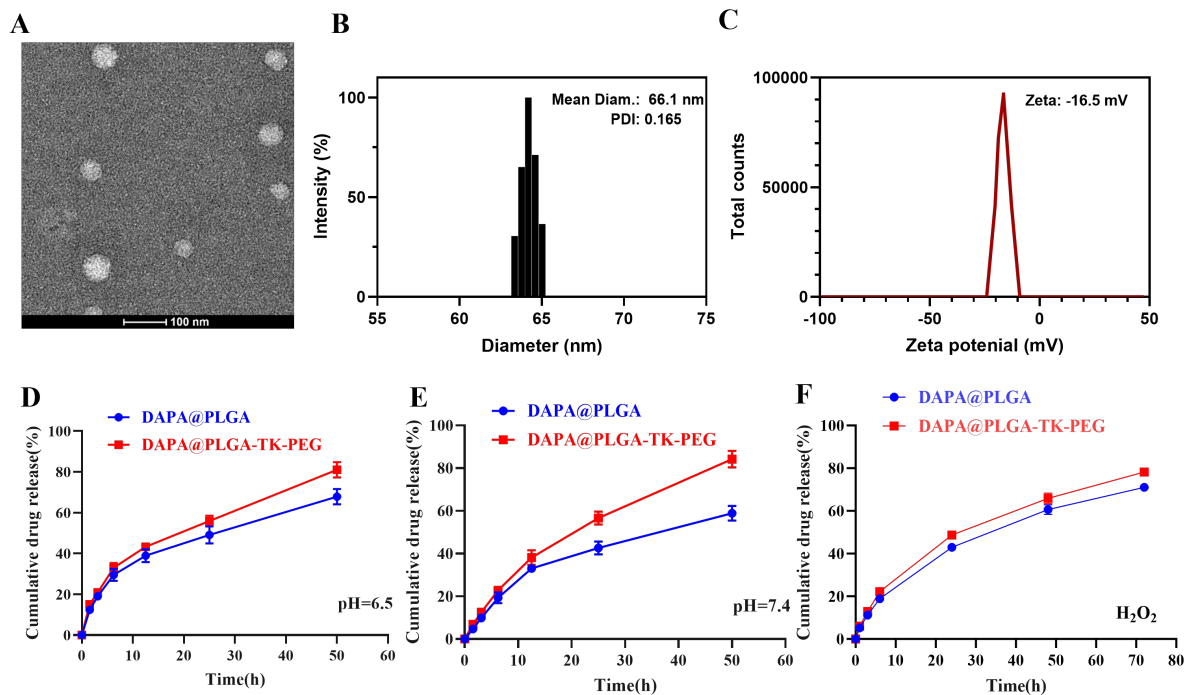


Fig. 1. Analysis of the characteristics and *in vitro* drug release properties of DAPA@NPs. (A) TEM image depicting the morphology of DAPA@NPs. Scale bar: 100 nm. (B) Size distribution profile of DAPA@NPs. (C) Zeta potential measurement of DAPA@NPs. (D) Release profiles of DAPA from PLGA and PLGA-TK-PEG in pH 6.5 solution. (E) Release profiles of DAPA from PLGA and PLGA-TK-PEG in pH 7.4 solution. (F) Release profiles of DAPA from PLGA and PLGA-TK-PEG after H₂O₂ treatment (n = 3). TEM, transmission electron microscopy; DAPA, dapagliflozin; NP, nanoparticle; TK, thioketal; PLGA, poly(lactic-co-glycolic acid); PEG, polyethylene glycol; PDI, polydispersity index.

ferent forms of DAPA improved myocardial fiber organization and reduced necrosis and inflammatory cell infiltration. DAPA@PLGA-TK-PEG demonstrated superior therapeutic effects compared with DAPA@PLGA, and DAPA@PLGA showed better efficacy than free DAPA. Masson's trichrome staining and Sirius red staining indicated increased collagen fiber deposition in the myocardial tissues (Fig. 2B,C). Compared with the control group, the model group exhibited elevated collagen fiber deposition, which was significantly attenuated following treatment with DAPA@NPs, with DAPA@PLGA-TK-PEG showing the most pronounced therapeutic effect.

We also assessed oxidative stress levels in the myocardial tissues of each mouse group. Compared with the control group, the model group showed significantly elevated levels of malondialdehyde (MDA) and protein carbonyl (PCO) as well as reduced activities of the antioxidant enzymes superoxide dismutase (SOD) and catalase (CAT) ($p < 0.001$, Fig. 2D–G). Treatment with free DAPA, DAPA@PLGA, and DAPA@PLGA-TK-PEG improved these oxidative stress biomarkers in DCM mice, with DAPA@PLGA-TK-PEG demonstrating the most significant improvements ($p < 0.01$, and $p < 0.001$) (Fig. 2D–G). These findings highlight the antioxidative stress effects of DAPA@NP.

DAPA@NP Alleviates Mitochondrial Damage and Iron Death in DCM Mice

Changes in mitochondrial morphology and structure in myocardial tissue were observed using TEM. The ultrastructure of myocardial tissue in the model group mice showed significant alterations, including myofibril fragmentation, mitochondrial swelling, partial outer membrane rupture, and disappearance or fragmentation of mitochondrial cristae (Fig. 3A). However, after treatment with DAPA@NPs, the disarrayed mitochondrial structure in DCM mice was effectively improved, with few swollen mitochondria, intact inner and outer membranes, and increased mitochondrial cristae. The improvement effect of DAPA@PLGA-TK-PEG was the most pronounced (Fig. 3A). Correspondingly, the inadequate ATP levels in the myocardial tissue of DCM mice were partially improved after treatment with different forms of DAPA ($p < 0.05$, $p < 0.01$, and $p < 0.001$; Fig. 3B). Hence, to some extent, DAPA can reduce mitochondrial damage and protect mitochondrial function.

Given the close association between cardiac iron homeostasis and heart disease, we investigated key factors related to iron metabolism and ferroptosis. In mice in the model group, we observed significant increases in total iron and Fe²⁺ levels and elevated expression of the TfR1 protein

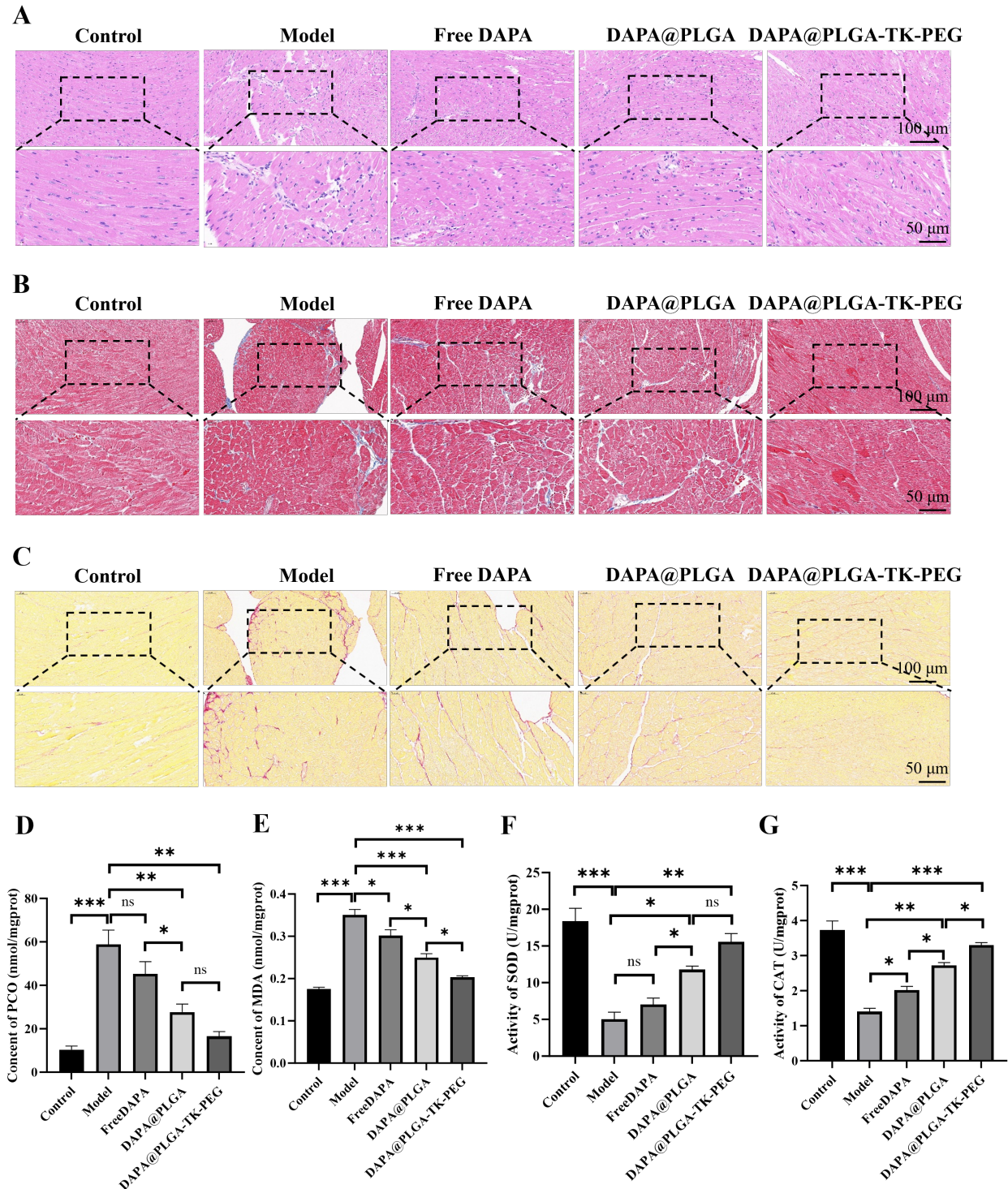


Fig. 2. DAPA@NP attenuates oxidative stress and fibrosis in diabetic myocardial tissue. (A) HE staining outcomes of myocardial tissue. Scale bar: 50 μm or 100 μm . (B) Masson staining outcomes of myocardial tissue. Scale bar: 50 μm or 100 μm . (C) Sirius red staining outcomes of myocardial tissue. Scale bar: 50 μm or 100 μm . (D–G) Quantification of PCO, MDA, SOD, and CAT levels in myocardial tissue. N = 3. ns, no statistical difference, * $p < 0.05$, ** $p < 0.01$, *** $p < 0.001$. HE, hematoxylin-eosin; PCO, protein carbonyl; MDA, malondialdehyde; SOD, superoxide dismutase; CAT, catalase.

($p < 0.001$) (Fig. 3C–H). The GSH levels and FPN protein expression significantly decreased in the model group than in normal mice ($p < 0.01$ and $p < 0.001$; Fig. 3C–H). Fol-

lowing treatment with various forms of DAPA@NPs, total iron and Fe^{2+} levels as well as TfR1 protein expression decreased, whereas GSH levels and FPN protein expression

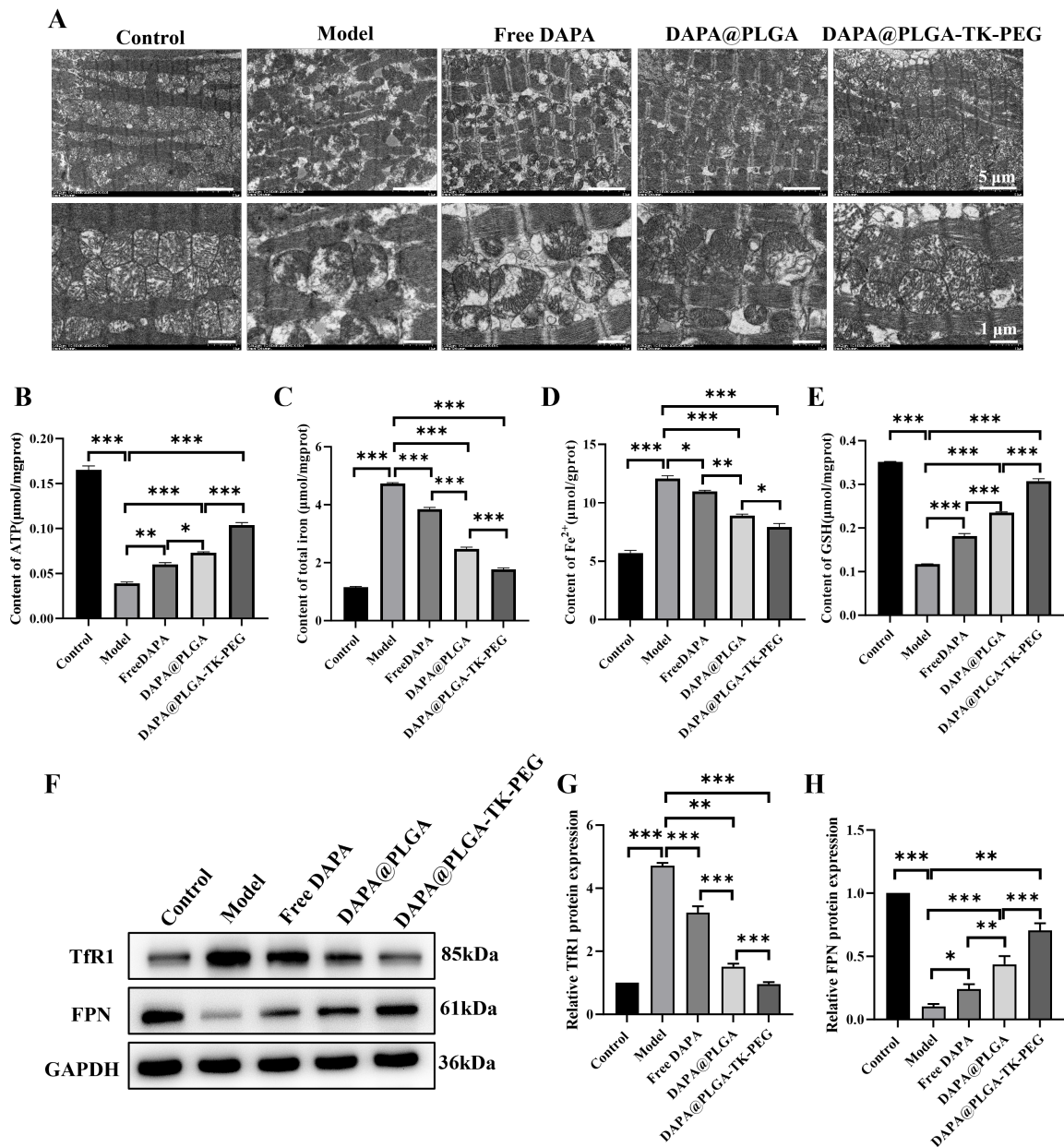


Fig. 3. DAPA@NPs inhibit mitochondrial damage and iron death in diabetic mice. (A) Observation of mitochondrial morphology and structure in cardiac tissues by TEM. Scale bar: 1 μm or 5 μm. (B–E) ELISA kit was used to determine (B) ATP content; (C) total iron; (D) Fe²⁺ and (E) GSH in cardiac tissues. (F–H) Expression levels of iron death and iron metabolism-related proteins TfR1 and FPN were analyzed by Western blot assay. N = 3. **p* < 0.05, ***p* < 0.01, ****p* < 0.001. ATP, adenosine triphosphate; GSH, glutathione; FPN, ferroportin; TfR1, transferrin receptor protein 1; GAPDH, glyceraldehyde-3-phosphate dehydrogenase; ELISA, enzyme-linked immunosorbent assay.

increased (*p* < 0.05, *p* < 0.01, and *p* < 0.001; Fig. 3C–H, **Supplementary file**). Notably, DAPA@PLGA-TK-PEG exhibited the most significant therapeutic effects. These findings indicate the presence of ferroptosis in DCM mice. Hence, DAPA@NPs can mitigate ferroptosis by regulating iron homeostasis.

DAPA@NPs Alleviate High Glucose-Induced Oxidative Stress and Mitochondrial Damage in Myocardial Cells

Building upon animal experiments, we further explored how DAPA@NP protects AC16 cells from high glucose-induced damage. Initially, AC16 cells were exposed to different formulations of DAPA (free DAPA, DAPA@PLGA, DAPA@PLGA-TK-PEG) in high-glucose culture medium for 24 hours, and cell viability was assessed using a CCK-8 assay kit. The results revealed

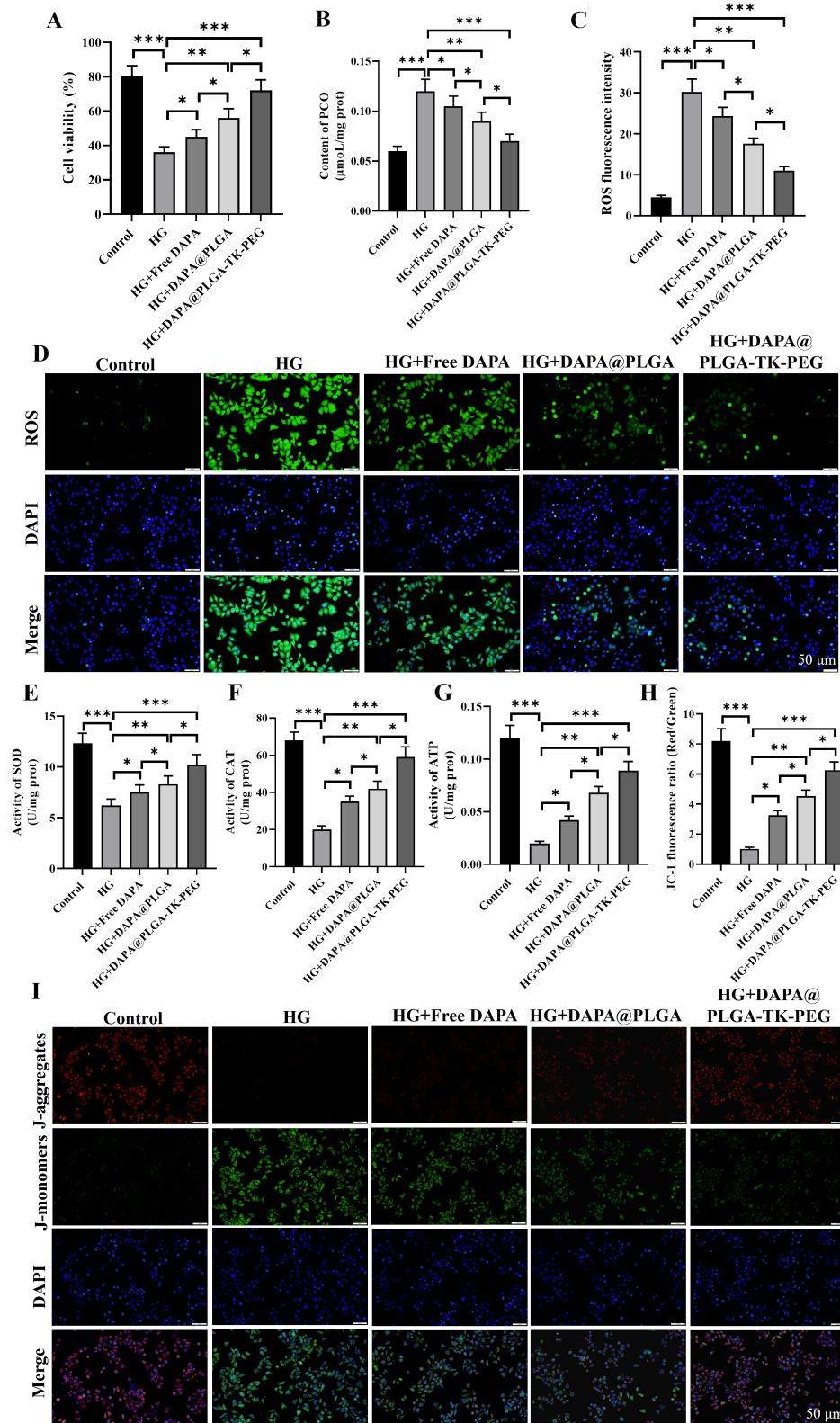


Fig. 4. DAPA@NPs alleviate oxidative stress and mitigates mitochondrial damage caused by HG. (A) The effect of DAPA@NP on the viability of AC16 cells. (B) PCO content. (C,D) Fluorescence intensity and images of intracellular ROS stained with DCFH-DA. Scale bar: 50 μm. (E–G) Levels of SOD, CAT, and ATP in AC16 cells of each group. (H,I) JC-1 fluorescence ratio and images. Scale bar: 50 μm. N = 3. **p* < 0.05, ***p* < 0.01, ****p* < 0.001. JC-1, 5,5',6,6'-Tetrachloro-1,1',3,3'-tetraethyl-imidacarbocyanine; DCFH-DA, 2',7'-dichlorodihydrofluorescein diacetate; ROS, reactive oxygen species; DAPI, 4',6-Diamidino-2'-phenylindole.

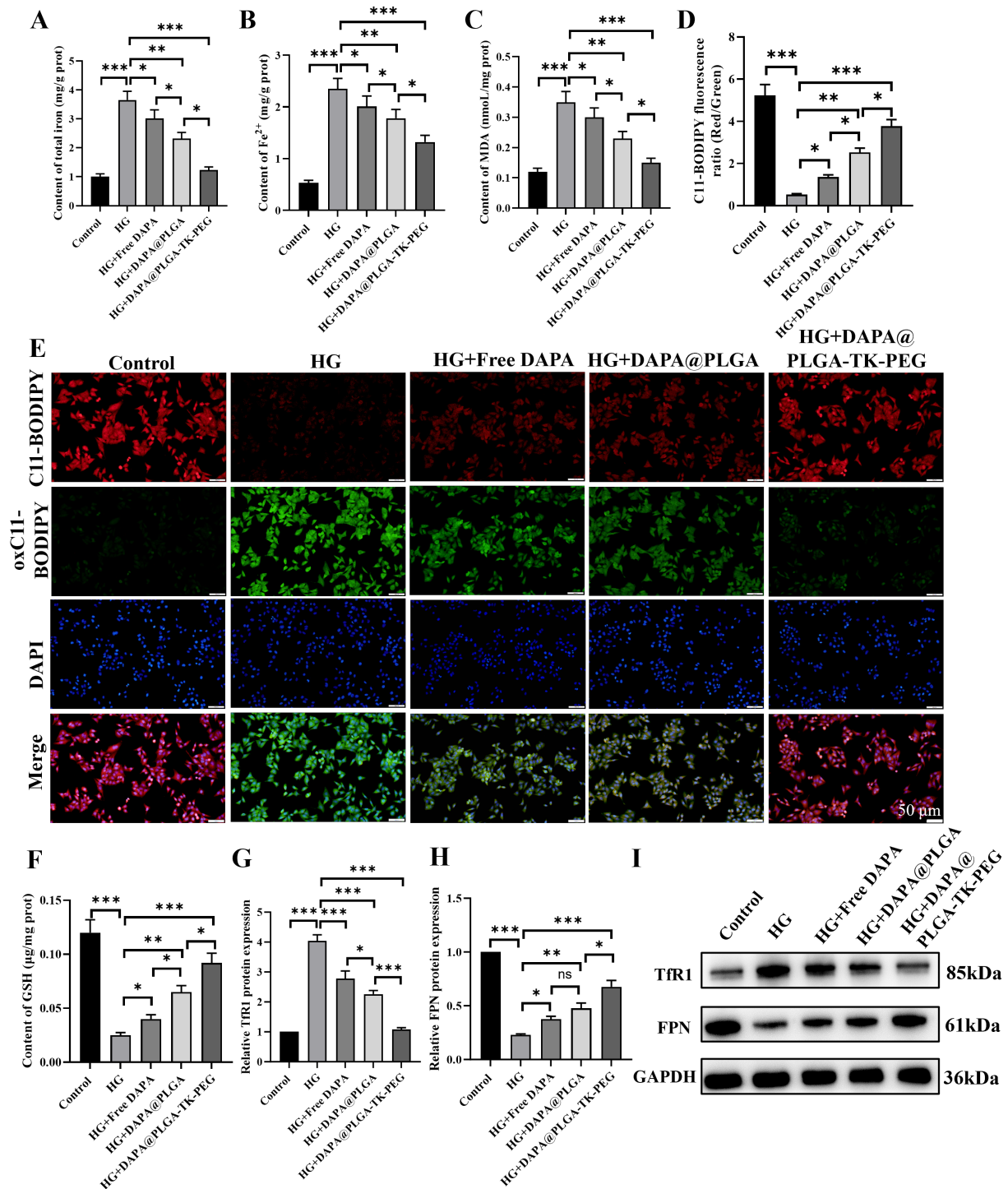


Fig. 5. DAPA@NP alleviates high glucose-induced iron death in myocardial cells. (A) Levels of total iron and (B) Fe²⁺ content in AC16 cells of each group. (C) Levels of MDA. (D,E) Ratio and fluorescence images of C11-BODIPY (non-oxidized)/oxC11-BODIPY (oxidized) staining. Scale bar: 50 μm. (F) Levels of GSH. (G–I) Protein levels of Tfr1 and FPN in AC16 cells analyzed by Western blot. N = 3. ns, no statistical difference, **p* < 0.05, ***p* < 0.01, ****p* < 0.001. BODIPY, boron-dipyrromethene.

that under high glucose conditions, cell viability in the HG group decreased by approximately 40 % compared to the control group. Moreover, treatment with various forms of DAPA significantly enhanced AC16 cell viability in a dose-dependent manner compared to the HG

group (*p* < 0.001). Specifically, cell viability was the highest in the DAPA@PLGA-TK-PEG group, followed by DAPA@PLGA and Free DAPA (*p* < 0.05, *p* < 0.01, and *p* < 0.001) (Fig. 4A).

As depicted in Fig. 4B–D, the levels of reactive oxygen species (ROS) and protein carbonyl (PCO) were significantly elevated in HG-treated cells compared with those in the control group. By contrast, the activities of antioxidant enzymes superoxide dismutase (SOD) and catalase (CAT) were notably decreased ($p < 0.001$). Consistent with the animal model findings, different forms of DAPA@NP effectively mitigated high glucose-induced oxidative stress by reducing intracellular ROS and PCO levels and enhancing intracellular SOD and CAT activities ($p < 0.05$, $p < 0.01$, and $p < 0.001$) (Fig. 4B–F).

Mitochondria, crucial for energy metabolism and ROS regulation in myocardial cells, were adversely affected by high glucose in AC16 cells, leading to reduced ATP production and mitochondrial damage. Importantly, treatment with DAPA@NP formulations ameliorated the decrease in ATP production induced by high glucose ($p < 0.05$, $p < 0.01$, and $p < 0.001$) (Fig. 4G–I).

These findings underscore the antioxidant and mitochondrial protective effects of DAPA and highlight its potential therapeutic benefits in diabetic cardiomyopathy.

DAPA@NP Alleviates Iron Death in Myocardial Cells Induced by High Glucose

DAPA helps regulate myocardial iron balance in DCM mice, so we proceeded to investigate iron metabolism in AC16 cells. After exposure to high glucose, we observed increased iron accumulation in AC16 cells, as indicated by the elevated levels of total iron, Fe^{2+} , and MDA ($p < 0.001$) (Fig. 5A–C). After intervention with DAPA nanoformulations, the levels of high glucose-induced iron deposition and MDA significantly decreased, with the most significant reduction observed in the DAPA@PLGA-TK-PEG group ($p < 0.05$, $p < 0.01$, and $p < 0.001$) (Fig. 5A–C). Excessive intracellular lipid peroxidation often accompanies iron overload. C11-BODIPY staining revealed that oxC11-BODIPY levels were markedly elevated in the HG group compared with that in the control group ($p < 0.001$, Fig. 5D,E). However, treatment with free DAPA, DAPA@PLGA, or DAPA@PLGA-TK-PEG significantly reduced oxC11-BODIPY levels, with the most pronounced decrease observed in the DAPA@PLGA-TK-PEG group ($p < 0.05$, $p < 0.01$, and $p < 0.001$; Fig. 5D,E). Additionally, GSH levels in AC16 cells were suppressed in the HG group, but intervention with DAPA@NPs effectively restored the level ($p < 0.05$, $p < 0.01$, and $p < 0.001$; Fig. 5F).

Analysis from Fig. 5G–I (Supplementary file) demonstrated that HG exposure significantly upregulated TfR1 protein expression and downregulated FPN protein expression. Conversely, treatment with DAPA@NP formulations significantly decreased TfR1 expression and increased FPN expression ($p < 0.05$, $p < 0.01$, and $p < 0.001$). These findings highlight the role of DAPA@NP in mitigating iron overload and improving iron metabolism-associated cellular damage.

Discussion

This study aimed to evaluate the efficacy of DAPA loaded in NPs in treating DCM and assess its potential value by comparing it with relevant research findings. We successfully synthesized DAPA@NPs, which exhibited regular morphology, spherical shape, smooth surface, high encapsulation efficiency, and superior performance. This finding is consistent with previous research that indicated the crucial importance of the morphology and size of NPs for their drug loading and release properties [20–22]. Furthermore, the drug release rate of TK-modified PLGA nanoparticles (DAPA@PLGA-TK-PEG) was significantly higher than that of unmodified PLGA nanoparticles (DAPA@PLGA) in solutions with pH values of 6.5 and 7.4. In previous works, the morphology and size of NPs are critical to their drug loading and release properties, resulting in increased drug release through the formation of synthetic nanoparticles through PLGA and PLGA-TK-PEG [23,24].

In vivo experiments, we observed the superiority of DAPA@PLGA-TK-PEG in improving myocardial injury in DCM mice, manifested by alleviating myocardial fiber disarray, reducing the number of necrotic or inflammatory cells, and decreasing collagen deposition. This study supports the potential of surface-modified nanocarriers in improving myocardial lesions. Further biological evaluations showed that treatment with DAPA@PLGA-TK-PEG significantly reduced the levels of oxidative stress in the myocardium of DCM mice and improved mitochondrial structure and function. Oxidative stress secondary to transient or sustained increases in steady-state reactive oxygen species (ROS) levels in the heart leads to disruption of signaling pathways and oxidative modification of cell components, which can subsequently lead to cell dysfunction and even induced cell death through necrosis or apoptosis [25,26]. Treatment with DAPA@PLGA-TK-PEG could regulate iron metabolism and reduce the occurrence of iron death. Combined with previous reports supporting the potential of surface modified nanocarriers to improve cardiomyopathy, the present study demonstrated the role of nanocoated drugs in DCM. In addition, high blood sugar is not the only cause of diabetic heart complications. Lipotoxicity [27] and increased oxidation of free fatty acids [28] also lead to oxidative stress, mitochondrial and endoplasmic reticulum (ER) stress, and activation of pro-inflammatory signals [29–31]. Mitochondrial damage leads to ROS production and enhanced activation of nucleotide-binding oligomerization domain, leucine rich repeat and pvrin domain containing protein (NLRP) 3 inflammasome [32], which in turn may promote or exacerbate cardiac fibrosis.

Significant progress has been made in the application of nanocarriers in the treatment of heart diseases. Zhang *et al.* [33] reported a nanocarrier similar to DAPA@PLGA-TK-PEG, which successfully alleviated myocardial injury *in vivo* experiments and demonstrated superior drug release

kinetics. When polyethylene glycol (PEG) is exposed to elevated ROS levels, these joints undergo degradation or solubility changes that trigger the controlled release of the encapsulated drug [34]. Thioketal (TK) is unstable under O_2^- and H_2O_2 conditions. This degradation mechanism has been widely used to develop ROS-responsive materials for diseases characterized by high ROS microenvironments [35,36]. These findings further validate the potential value of nanocarriers in the treatment of heart diseases. Furthermore, research on the regulation of iron metabolism by nanocarriers is also relevant to our findings. Iron cell apoptosis is a specific type of cell death characterized by iron dependence and lipid peroxidation; it can lead to elevated intracellular ROS levels and may promote the occurrence and development of DCM [37]. Another study showed that mice fed with high-iron diet resulted in severe heart muscle damage and had typical iron apoptotic molecular features, including increased lipid peroxidation and reduced GSH levels [38]. The results of this study demonstrate the role of nanocarriers in regulating iron homeostasis. In addition, PLGA is currently the most safe vehicle for drug delivery [39].

This study conducted a preliminary evaluation of the potential value of DAPA@PLGA-TK-PEG in the treatment of diabetic cardiomyopathy as well as compared and analyzed the findings with relevant research. However, this work still has some limitations.

First, this study mainly focused on evaluating the therapeutic effects of DAPA@PLGA-TK-PEG in animal models but lacked sufficient clinical data to support its effectiveness and safety in humans. In addition, the sample size of this study is currently small. Therefore, future research needs to conduct clinical trials to validate the feasibility and efficacy of its clinical application. The sample size should also be expanded, as too small a sample size may cause large errors or inaccuracies in the current research results.

Second, although we observed the positive effects of DAPA@PLGA-TK-PEG on alleviating myocardial injury, regulating oxidative stress, and iron metabolism, the specific mechanism of action remains unclear. Future research could delve deeper into the molecular mechanisms of DAPA@PLGA-TK-PEG in the treatment of diabetic heart disease to reveal the detailed mechanisms of its therapeutic effect.

Additionally, this study only considered the single application of DAPA@PLGA-TK-PEG in the treatment of DCM. Future research could explore its combined application with other drugs or treatment modalities to enhance treatment effectiveness.

Finally, although we optimized the preparation process of DAPA@PLGA-TK-PEG, some technical challenges persist, such as feasibility and stability issues in bulk production. Therefore, future research should optimize the preparation process to improve preparation efficiency and product stability.

Conclusions

Through comparison and analysis with previous relevant studies, we validate the potential value of DAPA@PLGA-TK-PEG as a treatment for DCM and provide strong support for its clinical application. However, despite some encouraging results, more clinical research is still needed to confirm its clinical efficacy and explore its mechanisms of action.

List of Abbreviations

DCM, diabetic cardiomyopathy; HF, heart failure; NP, nanoparticle; SGLT-2; sodium-glucose cotransporter-2; DAPA, dapagliflozin; SOD, superoxide dismutase; CAT, catalase; GSH, glutathione; MDA, malondialdehyde; PCO, protein carbonyl; TfR1, transferrin receptor protein 1; FPN, ferroportin; DCFH-DA, 2',7'-dichlorodihydrofluorescein diacetate; BODIPY, boron-dipyromethene; JC-1, 5,5',6,6'-Tetrachloro-1,1',3,3'-tetraethyl-imidacarbocyanine; T1D, type 1 diabetes; MRI, magnetic resonance imaging; TEM, transmission electron microscopy; DLS, dynamic light scattering; EE %, encapsulation efficiency; LC %, load capacity; STZ, streptozotocin; HE, hematoxylin-eosin; CCK-8, cell counting kit-8; ATP, adenosine triphosphate; BCA, bicinchoninic acid assay; ROS, reactive oxygen species; TK, thioketal; PLGA, poly(lactic-co-glycolic acid); PEG, polyethylene glycol; GAPDH, glyceraldehyde-3-phosphate dehydrogenase; ELISA, enzyme-linked immunosorbent assay.

Availability of Data and Materials

The datasets used and/or analysed during the current study were available from the corresponding author on reasonable request.

Author Contributions

CYL and FX designed the study. LRZ, CC and JYK collected and analyzed the data. CYL and TZ participated in drafting the manuscript. All authors conducted the study. All authors contributed to critical revision of the manuscript for important intellectual content. All authors gave final approval of the version to be published. All authors participated fully in the work, took public responsibility for appropriate portions of the content, and agreed to be accountable for all aspects of the work in ensuring that questions related to the accuracy or completeness of any part of the work were appropriately investigated and resolved.

Ethics Approval and Consent to Participate

All animal procedures were performed in accordance with the Guidelines for the Care and Use of Laboratory Animals of The Second Hospital of Shandong University. The study was approved by the Institutional Animal Care and Use Committee of The Second Hospital of Shandong University (KYLL2025336).

Acknowledgments

Not applicable.

Funding

General Project of Natural Science Foundation of Shandong Province (project number ZR2021MH067).

Conflict of Interest

The authors declare no conflict of interest.

Supplementary Material

Supplementary material associated with this article can be found, in the online version, at <https://doi.org/10.22203/eCM.v050a02>.

References

- [1] Lorenzo-Almorós A, Cepeda-Rodrigo JM, Lorenzo Ó. Diabetic cardiomyopathy. *Revista Clínica Española*. 2022; 222: 100–111. <https://doi.org/10.1016/j.rceng.2019.10.012>.
- [2] Peng C, Zhang Y, Lang X, Zhang Y. Role of mitochondrial metabolic disorder and immune infiltration in diabetic cardiomyopathy: new insights from bioinformatics analysis. *Journal of Translational Medicine*. 2023; 21: 66. <https://doi.org/10.1186/s12967-023-03928-8>.
- [3] Nakamura K, Miyoshi T, Yoshida M, Akagi S, Saito Y, Ejiri K, *et al*. Pathophysiology and Treatment of Diabetic Cardiomyopathy and Heart Failure in Patients with Diabetes Mellitus. *International Journal of Molecular Sciences*. 2022; 23: 3587. <https://doi.org/10.3390/ijms23073587>.
- [4] Zhao X, Liu S, Wang X, Chen Y, Pang P, Yang Q, *et al*. Diabetic cardiomyopathy: Clinical phenotype and practice. *Frontiers in Endocrinology*. 2022; 13: 1032268. <https://doi.org/10.3389/fendo.2022.1032268>.
- [5] Vergès B. Cardiovascular disease in type 1 diabetes: A review of epidemiological data and underlying mechanisms. *Diabetes & Metabolism*. 2020; 46: 442–449. <https://doi.org/10.1016/j.diabet.2020.09.001>.
- [6] Wong TC, Piehler KM, Kang IA, Kadakkal A, Kellman P, Schwartzman DS, *et al*. Myocardial extracellular volume fraction quantified by cardiovascular magnetic resonance is increased in diabetes and associated with mortality and incident heart failure admission. *European Heart Journal*. 2014; 35: 657–664. <https://doi.org/10.1093/eurheartj/ehu193>.
- [7] Tan Y, Zhang Z, Zheng C, Wintergerst KA, Keller BB, Cai L. Mechanisms of diabetic cardiomyopathy and potential therapeutic strategies: preclinical and clinical evidence. *Nature Reviews. Cardiology*. 2020; 17: 585–607. <https://doi.org/10.1038/s41569-020-0339-2>.
- [8] Udell JA, Jones WS, Petrie MC, Harrington J, Anker SD, Bhatt DL, *et al*. Sodium Glucose Cotransporter-2 Inhibition for Acute Myocardial Infarction: JACC Review Topic of the Week. *Journal of the American College of Cardiology*. 2022; 79: 2058–2068. <https://doi.org/10.1016/j.jacc.2022.03.353>.
- [9] Suzuki Y, Kaneko H, Okada A, Matsuoka S, Fujii K, Michihata N, *et al*. Kidney outcomes in patients with diabetes mellitus did not differ between individual sodium-glucose cotransporter-2 inhibitors. *Kidney International*. 2022; 102: 1147–1153. <https://doi.org/10.1016/j.kint.2022.05.031>.
- [10] Reid J, Rana K, Niman S, Sheikh-Ali M, Lewis T, Choksi RR, *et al*. Sodium-Glucose Cotransporter-2 (SGLT-2) Inhibitors for Cardiovascular Disease Prevention. *American Journal of Cardiovascular Drugs: Drugs, Devices, and Other Interventions*. 2020; 20: 419–429. <https://doi.org/10.1007/s40256-020-00397-y>.
- [11] Liu Z, Ma X, Ilyas I, Zheng X, Luo S, Little PJ, *et al*. Impact of sodium glucose cotransporter 2 (SGLT2) inhibitors on atherosclerosis: from pharmacology to pre-clinical and clinical therapeutics. *Theranostics*. 2021; 11: 4502–4515. <https://doi.org/10.7150/thno.54498>.
- [12] Guo Y, Mao Z, Ran F, Sun J, Zhang J, Chai G, *et al*. Nanotechnology-Based Drug Delivery Systems to Control Bacterial-Biofilm-Associated Lung Infections. *Pharmaceutics*. 2023; 15: 2582. <https://doi.org/10.3390/pharmaceutics15112582>.
- [13] Li S, Chen L, Fu Y. Nanotechnology-based ocular drug delivery systems: recent advances and future prospects. *Journal of Nanobiotechnology*. 2023; 21: 232. <https://doi.org/10.1186/s12951-023-01992-2>.
- [14] Yang J, Shang J, Yang L, Wei D, Wang X, Deng Q, *et al*. Nanotechnology-Based Drug Delivery Systems for Honokiol: Enhancing Therapeutic Potential and Overcoming Limitations. *International Journal of Nanomedicine*. 2023; 18: 6639–6665. <https://doi.org/10.2147/ijn.S431409>.
- [15] Saeidi Z, Giti R, Rostami M, Mohammadi F. Nanotechnology-Based Drug Delivery Systems in the Transdermal Treatment of Melanoma. *Advanced Pharmaceutical Bulletin*. 2023; 13: 646–662. <https://doi.org/10.34172/apb.2023.070>.
- [16] Narmani A, Jahedi R, Bakhshian-Dehkordi E, Ganji S, Nemati M, Ghahramani-Asl R, *et al*. Biomedical applications of PLGA nanoparticles in nanomedicine: advances in drug delivery systems and cancer therapy. *Expert Opinion on Drug Delivery*. 2023; 20: 937–954. <https://doi.org/10.1080/17425247.2023.2223941>.
- [17] Ghotbi Z, Haddadi A, Hamdy S, Samuel J, Lavasanifar A. Development of PLGA nanospheres decorated with hydrophobized mannan for active targeting of dendritic cells. *Plga-Based Nanoparticles for Targeting of Dendritic Cells in Cancer Immunotherapy and Immunomonitoring* (pp. 116–139). University of Alberta: Edmonton, Alberta. 2010.
- [18] Wang J, Li Y, Dong X, Wang Y, Chong X, Yu T, *et al*. A Micelle Self-Assembled from Doxorubicin-Arabinoside Conjugates with pH-Cleavable Bond for Synergistic Antitumor Therapy. *Nanoscale Research Letters*. 2017; 12: 73. <https://doi.org/10.1186/s11671-017-1836-z>.
- [19] Chen H, Tian J, He W, Guo Z. H₂O₂-activatable and O₂-evolving nanoparticles for highly efficient and selective photodynamic therapy against hypoxic tumor cells. *Journal of the American Chemical Society*. 2015; 137: 1539–1547. <https://doi.org/10.1021/ja511420n>.
- [20] Chen Y, Feng X. Gold nanoparticles for skin drug delivery. *International Journal of Pharmaceutics*. 2022; 625: 122122. <https://doi.org/10.1016/j.ijpharm.2022.122122>.
- [21] Neri M, Kang J, Zuidema JM, Gasparello J, Finotti A, Gambari R, *et al*. Tuning the Loading and Release Properties of MicroRNA-Silencing Porous Silicon Nanoparticles by Using Chemically Diverse Peptide Nucleic Acid Payloads. *ACS Biomaterials Science & Engineering*. 2022; 8: 4123–4131. <https://doi.org/10.1021/acsbomaterials.1c00431>.
- [22] Nikezić AVV, Bondžić AM, Vasić VM. Drug delivery systems based on nanoparticles and related nanostructures. *European Journal of Pharmaceutical Sciences: Official Journal of the European Federation for Pharmaceutical Sciences*. 2020; 151: 105412. <https://doi.org/10.1016/j.ejps.2020.105412>.
- [23] Stiepel RT, Pena ES, Ehrenzeller SA, Gallovic MD, Lifshits LM, Genito CJ, *et al*. A predictive mechanistic model of drug release from surface eroding polymeric nanoparticles. *Journal of Controlled Release: Official Journal of the Controlled Release Society*. 2022; 351: 883–895. <https://doi.org/10.1016/j.jconrel.2022.09.067>.
- [24] Hornsby TK, Kashkooli FM, Jakhmola A, Kolios MC, Tavakkoli JJ. Kinetic modelling of ultrasound-triggered chemotherapeutic drug release from the surface of gold nanoparticles. *Scientific Reports*. 2023; 13: 21301. <https://doi.org/10.1038/s41598-023-48082-9>.
- [25] De Geest B, Mishra M. Role of Oxidative Stress in Heart Failure:

- Insights from Gene Transfer Studies. *Biomedicines*. 2021; 9: 1645. <https://doi.org/10.3390/biomedicines9111645>.
- [26] Lushchak VI. Free radicals, reactive oxygen species, oxidative stresses and their classifications. *The Ukrainian Biochemical Journal*. 2015; 87: 11–18. <https://doi.org/10.15407/ubj87.06.011>.
- [27] Tsushima K, Bugger H, Wende AR, Soto J, Jenson GA, Tor AR, *et al*. Mitochondrial Reactive Oxygen Species in Lipotoxic Hearts Induce Post-Translational Modifications of AKAP121, DRP1, and OPA1 That Promote Mitochondrial Fission. *Circulation Research*. 2018; 122: 58–73. <https://doi.org/10.1161/circresaha.117.311307>.
- [28] Boudina S, Sena S, Theobald H, Sheng X, Wright JJ, Hu XX, *et al*. Mitochondrial energetics in the heart in obesity-related diabetes: direct evidence for increased uncoupled respiration and activation of uncoupling proteins. *Diabetes*. 2007; 56: 2457–2466. <https://doi.org/10.2337/db07-0481>.
- [29] Li S, Zhang L, Ni R, Cao T, Zheng D, Xiong S, *et al*. Disruption of calpain reduces lipotoxicity-induced cardiac injury by preventing endoplasmic reticulum stress. *Biochimica et Biophysica Acta*. 2016; 1862: 2023–2033. <https://doi.org/10.1016/j.bbadis.2016.08.005>.
- [30] Ertunc ME, Hotamisligil GS. Lipid signaling and lipotoxicity in metaflammation: indications for metabolic disease pathogenesis and treatment. *Journal of Lipid Research*. 2016; 57: 2099–2114. <https://doi.org/10.1194/jlr.R066514>.
- [31] Wende AR, Symons JD, Abel ED. Mechanisms of lipotoxicity in the cardiovascular system. *Current Hypertension Reports*. 2012; 14: 517–531. <https://doi.org/10.1007/s11906-012-0307-2>.
- [32] Mishra SR, Mahapatra KK, Behera BP, Patra S, Bhol CS, Panigrahi DP, *et al*. Mitochondrial dysfunction as a driver of NLRP3 inflammasome activation and its modulation through mitophagy for potential therapeutics. *The International Journal of Biochemistry & Cell Biology*. 2021; 136: 106013. <https://doi.org/10.1016/j.biocel.2021.106013>.
- [33] Zhang Y, Zhang H, Zhao F, Jiang Z, Cui Y, Ou M, *et al*. Mitochondrial-targeted and ROS-responsive nanocarrier *via* nose-to-brain pathway for ischemic stroke treatment. *Acta Pharmaceutica Sinica*. B. 2023; 13: 5107–5120. <https://doi.org/10.1016/j.apsb.2023.06.011>.
- [34] Xu Q, He C, Xiao C, Chen X. Reactive Oxygen Species (ROS) Responsive Polymers for Biomedical Applications. *Macromolecular Bioscience*. 2016; 16: 635–646. <https://doi.org/10.1002/mabi.201500440>.
- [35] Shen J, Jiao W, Yuan B, Xie H, Chen Z, Wei M, *et al*. Oral Curcumin-Thioketal-Inulin Conjugate Micelles against Radiation-Induced Enteritis. *Antioxidants*. 2024; 13: 417. <https://doi.org/10.3390/antiox13040417>.
- [36] Yao Y, Li A, Wang S, Lu Y, Xie J, Zhang H, *et al*. Multifunctional elastomer cardiac patches for preventing left ventricle remodeling after myocardial infarction *in vivo*. *Biomaterials*. 2022; 282: 121382. <https://doi.org/10.1016/j.biomaterials.2022.121382>.
- [37] Zhao Y, Pan B, Lv X, Chen C, Li K, Wang Y, *et al*. Ferroptosis: roles and molecular mechanisms in diabetic cardiomyopathy. *Frontiers in Endocrinology*. 2023; 14: 1140644. <https://doi.org/10.3389/fendo.2023.1140644>.
- [38] Sawicki KT, De Jesus A, Ardehali H. Iron Metabolism in Cardiovascular Disease: Physiology, Mechanisms, and Therapeutic Targets. *Circulation Research*. 2023; 132: 379–396. <https://doi.org/10.1161/CIRCRESAHA.122.321667>.
- [39] Motawea A, Ahmed DAM, Eladl AS, El-Mansy AAE-R, Saleh NM. Appraisal of amiodarone-loaded PLGA nanoparticles for prospective safety and toxicity in a rat model. *Life Sciences*. 2021; 274: 119344. <https://doi.org/10.1016/j.lfs.2021.119344>.

Editor’s note: The Scientific Editor responsible for this paper was Pengyuan Wang.

Received: 10th October 2024; **Accepted:** 2nd January 2025; **Published:** 8th April 2025